




# Temperature Dependence of the Permeability of Sandstone Under Loading and Unloading Conditions of Confining Pressure

Yan-Hua Huang<sup>1,2</sup>  · Sheng-Qi Yang<sup>1</sup> · Shang-Yong Teng<sup>1</sup>

Received: 27 May 2019 / Accepted: 4 March 2020 / Published online: 14 April 2020  
© International Association for Mathematical Geosciences 2020

**Abstract** Rock permeability is a key parameter in evaluating the CO<sub>2</sub> storage capacity and injectivity in geologic CO<sub>2</sub> sequestration projects. To investigate the influences of confining pressure and testing temperature on rock permeability, seepage tests were carried out on four cylindrical sandstone specimens using a newly developed triaxial permeability measurement system. In this study, the confining pressure was loaded and unloaded stepwise between 10 and 30 MPa at different temperatures (25–90 °C). The experimental results showed that as the effective confining pressure increased in the loading process, sandstone permeability decreased nonlinearly. As the effective confining pressure decreased in the unloading process, permeability increased nonlinearly. Elevated temperature decreased the sandstone permeability, and the percentage reduction in permeability decreased with increasing temperature. Micropore space closure and thermal expansion were evidence of the permeability changes as the confining pressure and testing temperature were varied. The experimental results obtained in the seepage tests under the different confining pressures and elevated testing temperatures provide a reference for evaluating rock permeability in underground engineering.

---

✉ Sheng-Qi Yang  
yangsqi@hotmail.com

Yan-Hua Huang  
huangyh1219@163.com

<sup>1</sup> State Key Laboratory for Geomechanics and Deep Underground Engineering, School of Mechanics and Civil Engineering, China University of Mining and Technology, Xuzhou 221116, People's Republic of China

<sup>2</sup> School of Resources and Geosciences, China University of Mining and Technology, Xuzhou 221116, People's Republic of China

**Keywords** Sandstone · Permeability · Elevated temperature · Loading–unloading · Effective confining pressure

## 1 Introduction

The increasing emissions of greenhouse gases, especially carbon dioxide (CO<sub>2</sub>), into the atmosphere are a global environmental issue today. Many approaches have been proposed for reducing CO<sub>2</sub> emissions, including the use of renewable fuels, improved energy efficiency and carbon sequestration (Perera et al. 2012), among which CO<sub>2</sub> capture and storage is considered an effective way to reduce anthropogenic CO<sub>2</sub> emissions. Geological CO<sub>2</sub> sequestration (GCS) in sedimentary formations, depleted oil and gas reservoirs, deep unmineable coalbeds, and deep saline aquifers, is a large-scale storage solution (Li et al. 2003; Bachu and Adams 2003; Zhou et al. 2016; Huang et al. 2020c). Potential GCS media must have the following three characteristics: capacity, injectivity and confinement (Bachu 2008). Capacity is dependent on the caprock permeability, and injectivity is governed by the reservoir rock permeability (Cinar et al. 2009). Therefore, rock permeability is a key parameter for evaluating CO<sub>2</sub> storage capacity and injectivity in GCS.

In deep reservoirs, rock properties are often influenced by external loads (Ma et al. 2019b; Forcellini et al. 2018; Huang et al. 2020a). Rathnaweera et al. (2015) tested the permeability of brine-saturated sandstone under different stress conditions. The test results demonstrated that the permeability of saturated sandstone decreased as a power function with increasing confining pressure. Wang et al. (2017) measured the evolution of permeability of two sandstone specimens under cyclic loading and unloading of the confining pressure. Their experimental results revealed that the rock permeability in the unloading process was lower than that in the preceding loading process, and the relation between permeability and confining pressure was described by a power function. Zhang et al. (2018) conducted triaxial compression tests on crystalline sandstone specimens under loading and unloading conditions of the confining pressure. The sandstone permeability exhibited a nonlinear relation to the confining pressure along both the loading and unloading paths. However, the relationship between permeability and confining pressure was suitably described by an exponential function, which was different from what was reported in Wang et al. (2017). Therefore, the theoretical or empirical models describing the stress dependency of rock permeability are not unified. In addition, due to the elastic and nonelastic deformation induced by external stress, the evolution of permeability may be different in the loading and unloading processes, which needs to be further investigated.

On the other hand, the effect of the testing temperature on the change in rock permeability has been extensively investigated. Yang et al. (2017b) performed triaxial compression tests on red sandstone specimens after treatment at different temperatures. When the temperature increased from 25 to 800 °C, the permeability of the thermally treated sandstone first decreased slightly below 100 °C and subsequently increased notably after 500 °C. Ding et al. (2016) conducted water flow tests on sandstone specimens after high-temperature treatment to investigate the relationship between the permeability and treatment temperature. In their experiments, the permeability of

fractured sandstone first decreased below 400 °C, and then increased following an exponential function after 400 °C treatment. However, the above-mentioned studies were all conducted after high-temperature treatment, which cannot truly represent practical conditions. To overcome this shortcoming, Zhao et al. (2010) developed a servo-controlled testing system, which was used to measure permeability under real-time high-temperature conditions. Their experimental results showed that the gas permeability of coal specimens remained almost unchanged below 350 °C, but notably increased above 350 °C. Compared to the studies performed under relatively higher temperature conditions, the number of studies conducted in the temperature range of 25–100 °C influence is limited. De Silva et al. (2017) investigated the permeability of sandstone specimens at high temperatures in the range of 24 to 54 °C in 10 °C increments. Based on their experimental results, they concluded that sandstone permeability decreased with increasing temperature, and the reduction rate was high when the injection and confining pressure were low. Guo et al. (2017) conducted permeability measurement tests on four rock specimens at different intrinsic permeability levels and elevated temperatures. Their experiments revealed that the permeabilities of four fractured or unfractured rock specimens decreased when the temperature increased from 20 to 100 °C in intervals of 20 °C, which is consistent with the previous results of De Silva et al. (2017). However, regarding the permeability behavior of rock subjected to temperatures above 50 °C, little information is available in the literature.

From the abovementioned studies, the effects of the confining pressure and testing temperature on rock permeability have been separately investigated. However, regarding the rock permeability evolution behavior under different confining pressures and testing temperatures, little information has been previously reported in the literature. Therefore, to better understand the permeability response of reservoir rock under stress and elevated temperature conditions, in this study, seepage tests were carried out on sandstone specimens at a range of temperatures (25–90 °C) and confining pressures (10–30 MPa). The influences of the loading–unloading process and testing temperature on the evolution of the permeability of sandstone specimens were analyzed. Finally, the mechanisms of the confining pressure and elevated temperature underlying the permeability variation were examined. The experimental results are expected to provide a reference for the evaluation of the rock permeability in underground engineering.

## 2 Experimental Methodology

### 2.1 Testing System

A newly developed triaxial permeability measurement system was used in this study. The testing system consisted of a triaxial cell, a heating system, a pressure pump, a compressed CO<sub>2</sub> system and an acquisition system (Fig. 1a). The confining pressure and axial stress applied on the specimen was controlled by the pressure pump, and the maximum external stress was 60 MPa. The CO<sub>2</sub> injection pressure was increased by the pressure increment system and could reach 60 MPa. Both the CO<sub>2</sub> before injection and the rock specimen were located in the heating system, whose capacity was 150 °C. The gas flow rate at the outlet was recorded by a computer. During the

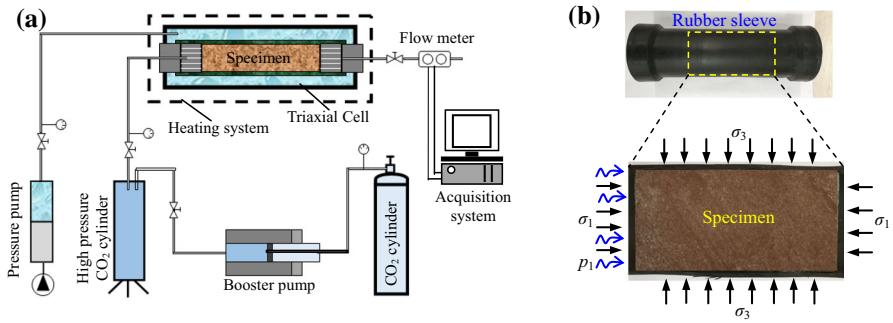


**Fig. 1** Testing equipment. **a** Schematic diagram of the test system, **b** schematic diagram of the flow test

test, the rock specimen was installed in the triaxial cell, and axial stress was applied in the horizontal direction, while confining pressure was applied in the circumferential direction. Moreover, the gas was injected upstream, as shown in Fig. 1b.

## 2.2 Sandstone Material

Sandstone is frequently encountered in underground engineering, and its properties have received much attention (Ma et al. 2019a; Huang et al. 2019, 2020b). In this study, outcrop sandstone was collected in Shandong Province, China. The sandstone was cored as a cylinder with a diameter of 50 mm and height of 100 mm. Four cylindrical specimens were used in the permeability tests. As shown in Fig. 2, the first two specimens (marked as RZS-A1 and RZS-B1) with a dark red color were cored from one sandstone block. The sandstone is a fine-grained heterogeneous material with a connected porosity of 6.88% and a bulk density of 2450 kg/m<sup>3</sup>. Boundary cracks, but no pores, were observed in the sandstone under the optical microscopy (Fig. 3a–b). The minerals in the sandstone were quartz, K-feldspar, plagioclase, calcite, dolomite, hematite and clay minerals according to X-ray diffraction (Yang et al. 2017a).

As shown in Fig. 2, the last two specimens (marked as LYS-A1 and LYS-B1) with a red color were cored from another sandstone block. The microstructure indicated that the rock was a fine- to medium-grained sandstone with a bulk density of 2450 kg/m<sup>3</sup>. Similar to the above two sandstone specimens, boundary cracks but no pores were observed in these two sandstone specimens under optical microscopy (Fig. 3c–d). The minerals in the sandstone were mainly quartz, K-feldspar, plagioclase and clay minerals. Table 1 summarizes the detailed geometrical parameters of the four sandstone specimens for the permeability tests.

## 2.3 Experimental Procedure

Figure 4 illustrates the flowchart of the permeability test for the rock specimens. Before the permeability test, all the prepared sandstone specimens were oven-dried. The experimental procedure is described below. The axial stress  $\sigma_1$  and confining

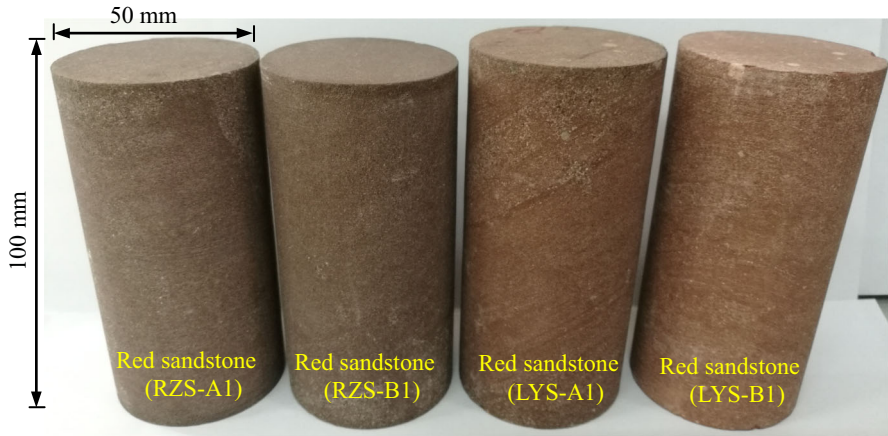


**Fig. 2** The four cylindrical sandstone specimens used in this study

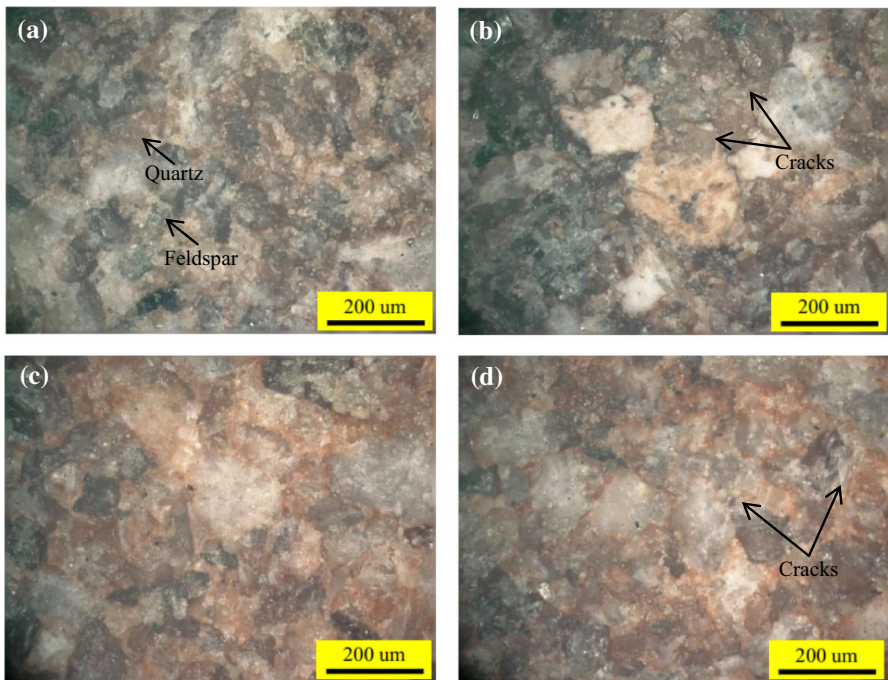


**Fig. 3** Surface images of the different sandstone specimens before the permeability test based on optical microscopy. **a** Specimen RZS-A1, **b** specimen RZS-B1, **c** specimen LYS-A1, and **d** specimen LYS-B1

pressure  $\sigma_3$  were first applied on the specimen to ensure that the specimen was under a uniform hydrostatic stress ( $\sigma_1 = \sigma_3 = 10$  MPa), and were constantly maintained during the whole test. Then, the testing temperature was increased to the designed value and maintained for 2 h before the permeability measurement test. The confining pressure was first loaded from 10 to 30 MPa and then unloaded from 30 to 10 MPa

**Table 1** Geometrical parameters of the tested sandstone specimens

Specimen	$D$ (mm)	$H$ (mm)	$m$ (g)	$\rho$ (kg/m <sup>3</sup> )
RZS-A1	49.97	98.53	473.02	2,448
RZS-B1	49.92	99.23	475.49	2,448
LYS-A1	50.21	103.70	503.34	2,451
LYS-B1	50.18	104.30	505.37	2,450

$D$  diameter,  $H$  height,  $m$  mass,  $\rho$  density of specimen

**Table 2** Permeability testing conditions in this study

Specimen	$\sigma_1 = \sigma_3$ (MPa)	$P_1$ (MPa)	$\sigma_e$ (MPa)	$T$ (°C)
RZS-A1	10, 15, 20, 25, 30	4	8, 13, 18, 23, 28	25, 50, 70, 90
RZS-B1	10, 15, 20, 25, 30	4/6	8, 13, 18, 23, 28/7, 12, 17, 22, 27	25, 50, 70, 90
LYS-A1	10, 15, 20, 25, 30	6	7, 12, 17, 22, 27	25, 50, 70, 90
LYS-B1	10, 15, 20, 25, 30	6	7, 12, 17, 22, 27	25, 50, 70, 90

$\sigma_1$  axial stress,  $\sigma_3$  confining pressure,  $p_1$  injection pressure,  $\sigma_e$  effective confining pressure,  $T$  testing temperature

in intervals of 5 MPa. At each confining pressure stage, the volume flow through the specimen was measured under a constant CO<sub>2</sub> injection pressure. After one cycle of loading and unloading, the testing temperature was increased to the next value. The same loading–unloading process of the confining pressure series was repeated at 25, 50, 70 and 90 °C. Note that the highest temperature in this study was below 100 °C to avoid water vaporization because the confining pressure was applied on rock specimens through distilled water. The maximum confining pressure was 30 MPa to avoid any irreparable damage to the sandstone specimens during the loading and unloading process. Table 2 lists the detailed permeability testing conditions in the loading and unloading process.

Sandstone is a porous medium, and the flow law is often conducted on a macroscopic scale where Darcy's law is valid (Ekeleme and Agunwamba 2018). In this experiment, sandstone permeability was measured using the steady-state method and calculated with the well-known Darcy equation (Eq. 1) (Scheidegger 1958), which is suitable for rock whose permeability is  $\geq 10^{-7} \mu\text{m}^2$  (Davy et al. 2007)

$$k = \frac{2Qp_0\mu H}{(P_1^2 - P_2^2)A}, \quad (1)$$

where,  $Q$  is the flow rate,  $p_0$  is the atmospheric pressure,  $\mu$  is the gas viscosity,  $H$  is the specimen height,  $A$  is the cross-section area,  $P_1$  is the injection pressure, and  $P_2$  is the downstream pressure.

The effective confining pressure  $\sigma_e$  is defined as the difference between the confining and pore pressures (Yu et al. 2019) and calculated as Eq. (2) (Alam et al. 2014) when the steady-state flow method is used

$$\sigma_e = \sigma_3 - P_1/2. \quad (2)$$

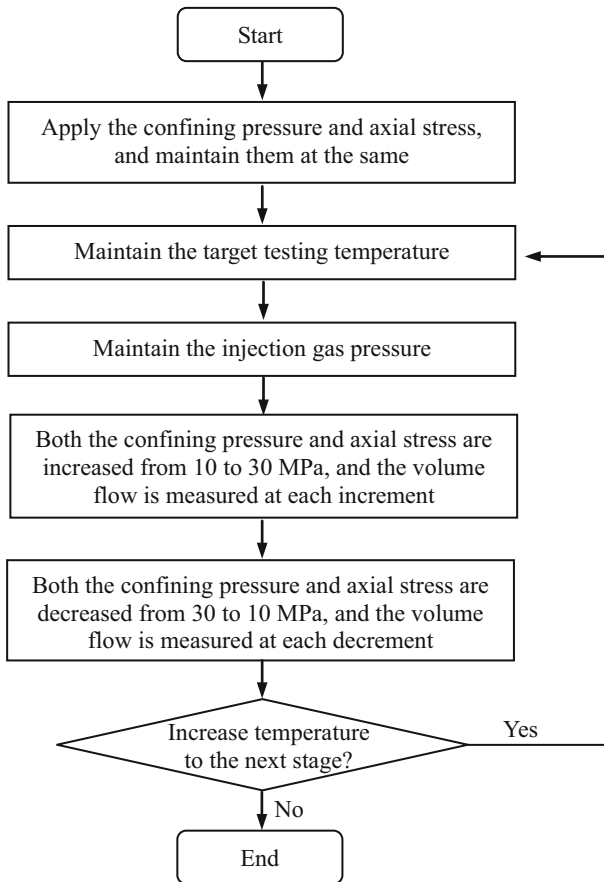


**Fig. 4** Flowchart of the permeability measurement tests for the rock specimens

### 3 Experimental Results

To evaluate the steady-state  $\text{CO}_2$  flow, the flow rate was recorded in real-time during the permeability test. Figure 5 shows the  $\text{CO}_2$  flow rate behavior of the sandstone specimens under the different conditions. In each permeability measurement test, the flow rate increased gradually and reached a steady state. Therefore, the permeability of the tested sandstone specimens could be measured using the steady-state method. The flow rate at the steady state was used to calculate the permeability. It is clear that the sandstone specimens cored from the same rock block attained different steady-state flow rates (Fig. 5a), which resulted from the heterogeneity of the sandstone material. The testing temperature and injection pressure had notable influences on the flow rate development. Under the same confining pressure, the steady-state flow rate was observed to decrease with increasing testing temperature (Fig. 5b). It is seen from Fig. 5c that the injection pressure enhanced the steady-state flow rate



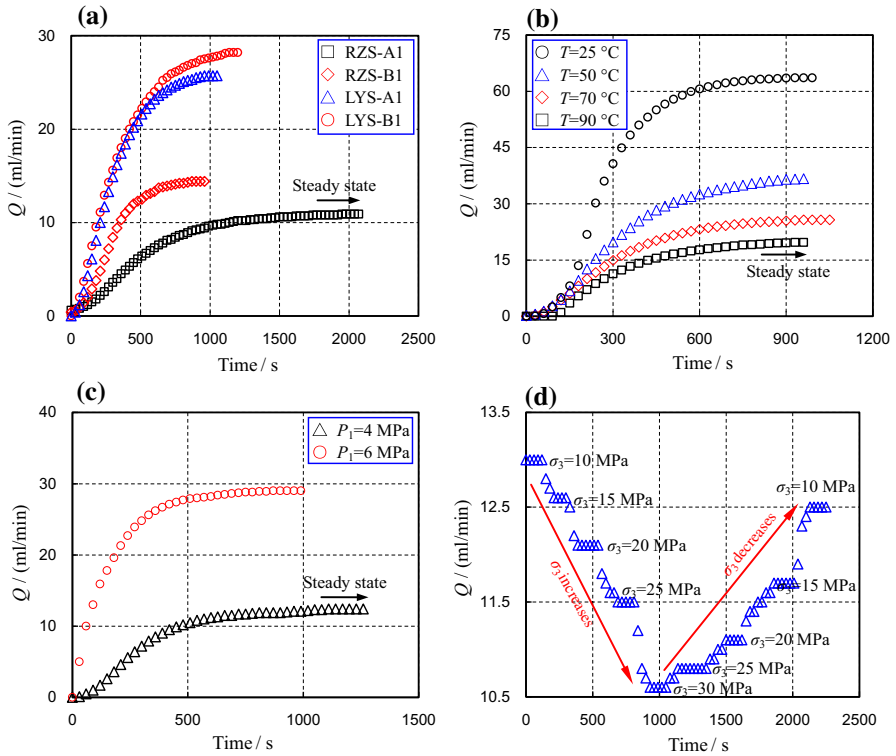


**Fig. 5** CO<sub>2</sub> flow rate of the sandstone during testing. **a** Different kinds of sandstone,  $\sigma_1 = \sigma_3 = 10$  MPa and  $T = 70$  °C, **b** different real-time temperatures,  $\sigma_1 = \sigma_3 = 10$  MPa and specimen LYS-A1, **c** different inlet pressures,  $\sigma_1 = \sigma_3 = 10$  MPa,  $T = 90$  °C and specimen RZS-B1, and **d** different confining pressures,  $T = 50$  °C and specimen RZS-A1

of the sandstone specimens. Furthermore, the steady flow rate decreased during the loading process and increased during the unloading process of the confining pressure (Fig. 5d).

Figure 6 shows the permeability results in the different sandstone specimens against the effective confining pressure. The influences of rock heterogeneity, injection pressure and confining pressure on the sandstone permeability were examined. (i) Under the same injection and effective confining pressures, the permeabilities of sandstone specimens RZS-A1 and RZS-B1 were different (Fig. 6a–b), resulting from the heterogeneity of the rock material. The difference in permeability between specimens LYS-A1 and LYS-B1 was minor under the same testing conditions, as shown in Fig. 6c–d. For example, the permeability of specimen LYS-A1 was  $5.671 \times 10^{-18}$  m<sup>2</sup>, while it was  $5.627 \times 10^{-18}$  m<sup>2</sup> for specimen LYS-B1 under  $\sigma_e = 7$  MPa at room temperature. (ii) The permeability of sandstone specimen RZS-B1 was generally lower compared to those of specimens LYS-A1 and LYS-B1 with the same injection pressure of 6 MPa, which was mainly a result of the differences in porosity and pore structure. (iii) When the tested sandstone specimens were subjected to different gas pressures,



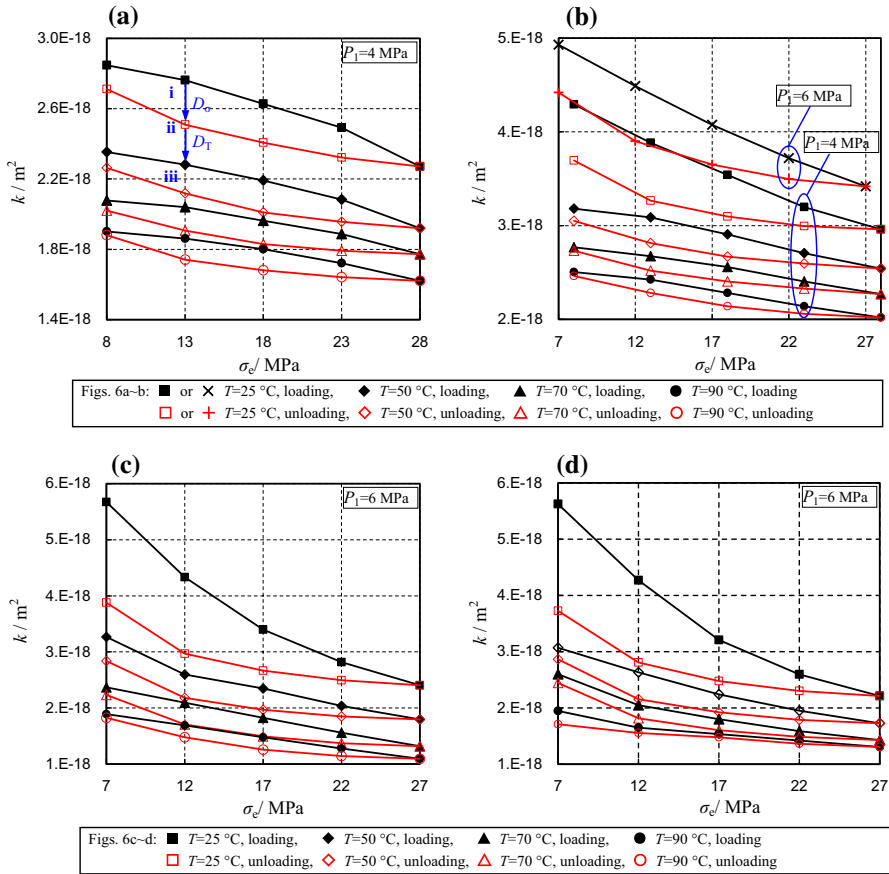


**Fig. 6** Relationship between the sandstone permeability and effective confining pressure. **a** Specimen RZS-A1, **b** Specimen RZS-B1, **c** Specimen LYS-A1, and **d** Specimen LYS-B1

the permeability changed. For example, the permeability of specimen RZS-B1 was  $4.293 \times 10^{-18} \text{ m}^2$  when the injection pressure was 4 MPa, and it changed to  $4.929 \times 10^{-18} \text{ m}^2$  when the injection pressure increased to 6 MPa under the same testing temperature ( $T=25$  °C) and confining pressure ( $\sigma_3 = 10$  MPa).

Although the permeability differed for the different sandstone specimens with respect to the different confining pressures, the evolution laws between the permeability and effective confining pressure were similar. The permeability of the sandstone specimens decreased with the effective confining pressure in the loading process. For example, the permeability of specimen RZS-A1 decreased from  $2.848 \times 10^{-18}$  to  $2.271 \times 10^{-18} \text{ m}^2$  when the effective confining pressure increased from 8 to 28 MPa at room temperature. Furthermore, as the effective confining pressure decreased, the permeability of the sandstone specimens increased gradually in the unloading process. For example, the permeability of specimen RZS-A1 increased from  $2.271 \times 10^{-18}$  to  $2.712 \times 10^{-18} \text{ m}^2$  when the effective confining pressure decreased from

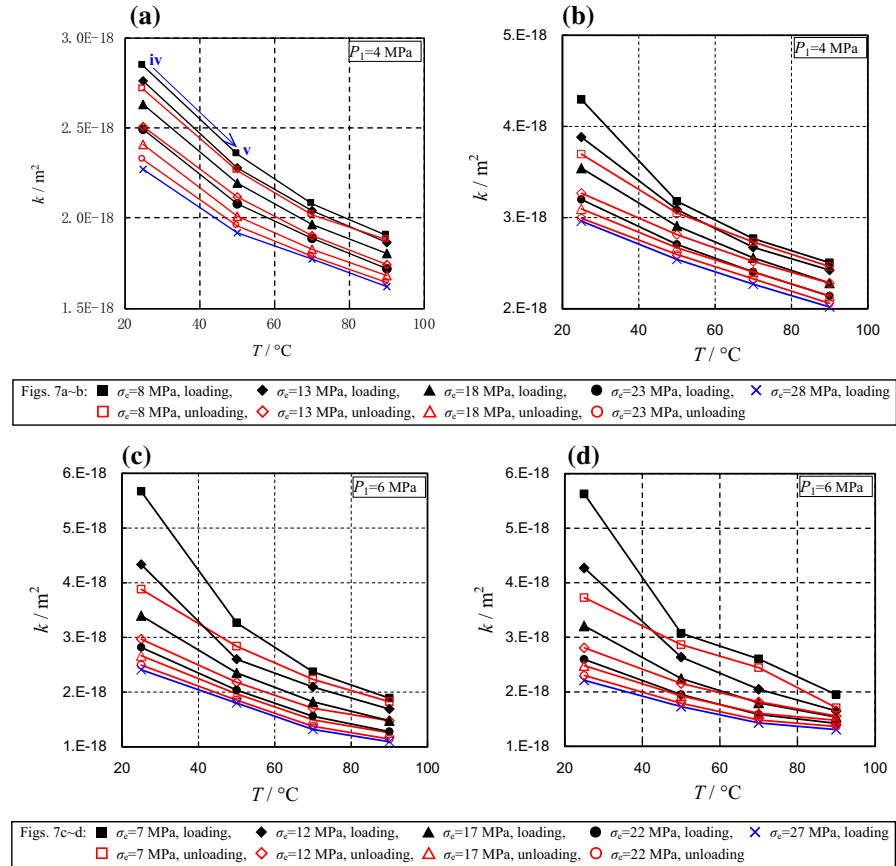


**Fig. 7** Relationship between the sandstone permeability and the testing temperature. **a** Specimen RZS-A1, **b** specimen RZS-B1, **c** specimen LYS-A1, and **d** specimen LYS-B1

28 to 8 MPa at room temperature. In addition, the permeability of the sandstone specimens in the unloading process was lower than that in the loading process. For example, the permeability of specimen RZS-A1 was  $2.407 \times 10^{-18} \text{ m}^2$  under  $\sigma_e = 18$  MPa in the unloading process, which was lower than the value of  $2.627 \times 10^{-18} \text{ m}^2$  under the same effective confining pressure in the loading process at room temperature.

Figure 7 shows the influence of the testing temperature on the permeability of the sandstone specimens under the loading and unloading conditions of the confining pressure. As the testing temperature increased, the permeability of the sandstone specimens decreased under each effective confining pressure. For example, the permeability of specimen RZS-A1 decreased from  $2.848 \times 10^{-18}$ ,  $2.354 \times 10^{-18}$ ,  $2.078 \times 10^{-18}$  and to  $1.901 \times 10^{-18} \text{ m}^2$  when the testing temperature was increased from 25, 50, 70 and to 90 °C under  $\sigma_e = 8$  MPa in the loading process. Moreover, the variation trends of the permeability were similar in the loading and unloading processes.

## 4 Discussion and Interpretation

### 4.1 Confining Pressure Effect on Permeability

Researchers have proposed exponential and power functions to describe the relationship between the permeability and confining pressure (Shi and Wang 1988; David et al. 1994; Rathnaweera et al. 2016). These two functions are expressed as Eq. (3)

$$\begin{aligned} k &= k_0 e^{a\sigma_e} \quad (\text{exponential function}), \\ k &= k_0 \sigma_e^b \quad (\text{power function}), \end{aligned} \quad (3)$$

where  $k_0$  is the initial permeability,  $\sigma_e$  is the effective confining pressure, and  $a$  and  $b$  are fitting parameters. From Fig. 6, the permeability of the sandstone specimens changed nonlinearly with the effective confining pressure regardless of the loading and unloading paths, which was consistent with the results of previous studies (Dong et al. 2010; Chen et al. 2016; Liu et al. 2016).

In the unloading process, the permeability was lower than that in the loading process under the same effective confining pressure, which meant that the permeability could not be recovered to reach its initial value after the confining pressure unloading. This is referred to as hysteretic behavior between the unloading and loading paths. In the past, a parameter named the damage rate ( $D_k$ ) was defined to evaluate the recovery extent of the permeability in the unloading process. The definition of  $D_k$  is given as Eq. (4) (He and Yang 2004)

$$D_k = \frac{k_0 - k_1}{k_0} \times 100\%, \quad (4)$$

where  $k_0$  is the initial permeability in the loading process, and  $k_1$  is the final permeability in the unloading process. Parameter  $D_k$  reflects the damage degree of the permeability under the initial and final confining pressures, but ignores the damage degree under the intermediate confining pressure. Therefore, a damage rate induced by stress ( $D_\sigma$ ) was defined in this study and expressed as Eq. (5).  $D_\sigma$  can reflect the unrecovered extent of the permeability in the unloading process

$$D_\sigma = \frac{k_L - k_{un}}{k_L} \times 100\%, \quad (5)$$

where,  $k_L$  is the permeability in the loading process, and  $k_{un}$  is the permeability under the same confining pressure as that of  $k_L$  in the unloading process. A schematic diagram of  $D_\sigma$  is shown in Fig. 6a, which is calculated from point i to point ii.

The values of  $D_\sigma$  calculated from Eq. (5) are listed in Table 3. Table 3 shows that as the effective confining pressure increased,  $D_\sigma$  decreased under the same testing temperature conditions. This indicates that the unrecovered permeability of the sandstone specimens was lower under the high confining pressure condition, because the structure of sandstone was denser after high stress compression.

To analyze the mechanism of loading and unloading of the confining pressure in changing the permeability of the sandstone specimens, we propose a conceptual dia-

**Table 3** Value of  $D_\sigma$  under testing condition

Specimen	$T$ (°C)	$\sigma_e$ (MPa)			
		8 (or 7)	13 (or 12)	18 (or 17)	23 (or 22)
RZS-A1	25	4.76	9.20	8.39	6.80
	50	3.85	7.14	8.26	6.09
	70	2.75	6.54	6.80	5.05
	90	1.05	6.45	6.67	4.65
RZS-B1	25	13.94	15.86	12.56	6.42
	50	4.02	8.88	8.18	4.05
	70	1.39	5.76	6.02	3.20
	90	1.61	5.83	6.19	3.77
LYS-A1	25	31.60	31.48	21.52	11.39
	50	13.08	16.10	16.29	9.17
	70	5.84	18.50	18.18	11.83
	90	3.55	12.50	14.94	10.53
LYS-B1	25	33.76	34.24	22.78	11.34
	50	6.67	18.24	14.29	8.22
	70	6.03	11.26	10.77	6.40
	90	12.32	5.81	3.75	4.05

gram of the microstructure of the sandstone material, as shown in Fig. 8. Microscopic cracks and pores occur in rock before loading (Esmailzadeh et al. 2017; Ahmadi and Molladavoodi 2018), which act as seepage channels (see point a). As the confining pressure increased, the pore volume of the sandstone decreased, resulting from the closure of pre-existing microcracks and pores (see points b and c). The shrinkage effect of the pore space caused a reduction in the gas seepage channels and eventually decreased the sandstone permeability under a high confining pressure. Furthermore, under a low confining pressure, the shrinkage extent was higher than that under a high confining pressure. This indicates that the permeability of the sandstone specimens decreased significantly under a low confining pressure but decreased slightly under a confining pressure. Therefore, the permeability showed a nonlinear development trend with the increase of confining pressure (Fig. 6). In the unloading process of the confining pressure, some of the elastically deformed microcracks and pores gradually recovered. However, the nonelastic pore volume shrinkage could not return to its original state after unloading of the confining pressure (see points  $a'$ ,  $b'$  and  $c'$ ). Consequently, this residual damage reduced the permeability of the sandstone specimens in the unloading process. This explains the lower permeability in the unloading process compared with that under the same confining pressure in the loading process.

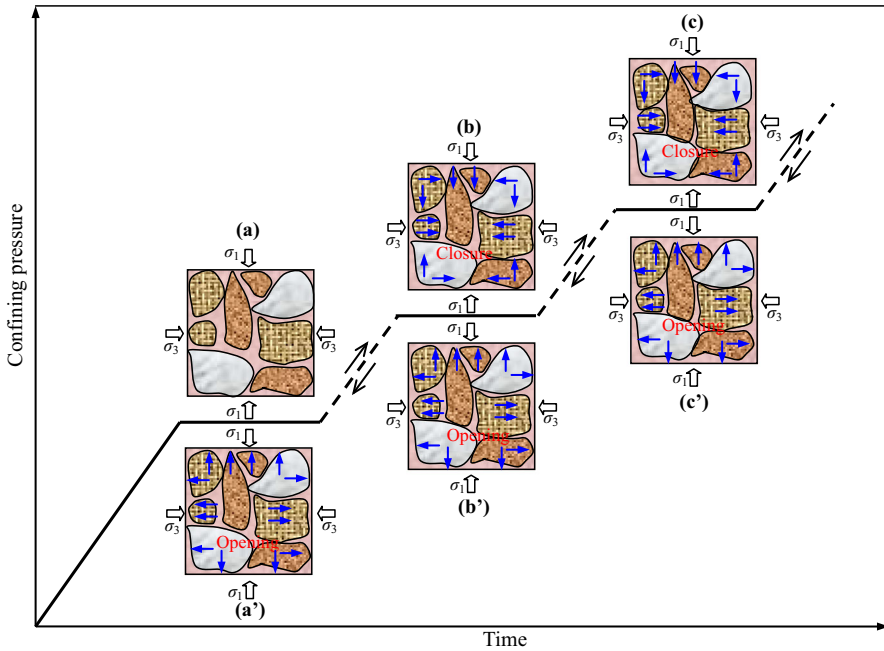


**Fig. 8** Diagram showing the change of microdefects in the sandstone specimens under loading and unloading of the confining pressure

**4.2 Temperature Effect on Permeability**

Nonlinear permeability evolution trends were observed when increasing the testing temperature process, which was more significant under low effective confining pressures, as shown in Fig. 7. Temperature-induced permeability reduction in rocks (sandstone and shale) at temperatures below 100 °C has been reported by Guo et al. (2017) and De Silva et al. (2017). However, the permeability first decreased and then increased according to Ju et al. (2016), who investigated fractured coal specimens. The difference in permeability between sandstone and coal specimens was due to CO<sub>2</sub> adsorption onto the coal matrix.

Researchers have suggested different functions to fit the correlation between the permeability and testing temperature. Exponential and power functions used to fit the permeability data are expressed as (Eq. 6)

$$\begin{aligned}
 k &= k_0 e^{cT} \quad (\text{exponential function}), \\
 k &= k_0 T^d \quad (\text{power function}),
 \end{aligned}
 \tag{6}$$

where  $k_0$  is the initial permeability,  $T$  is the testing temperature, and  $c$  and  $d$  are fitting parameters. However, the reduction in permeability with increasing temperature, as shown in Fig. 7, was induced by coupling of the loading–unloading process and testing temperature. For example, the reduction of  $4.94 \times 10^{-19} \text{ m}^2$  ( $2.848 \times 10^{-18}$ – $2.354 \times 10^{-18} \text{ m}^2$ ) under  $\sigma_e = 8 \text{ MPa}$  from point iv to point v (as marked in Fig. 7a) was the

**Table 4** Value of  $D_T$  under each testing condition

Specimen	$T$ (°C)	$\sigma_e$ (MPa)				
		8 (or 7)	13 (or 12)	18 (or 17)	23 (or 22)	28 (or 27)
RZS-A1	50	13.20	9.05	8.97	10.32	15.49
	70	8.22	3.74	2.33	3.52	7.65
	90	5.91	2.37	1.58	3.95	8.56
RZS-B1	50	13.94	5.47	6.15	9.65	14.16
	70	9.24	5.00	4.12	7.35	10.65
	90	8.32	3.83	5.10	8.03	11.03
LYS-A1	50	15.77	12.46	11.85	18.35	25.31
	70	16.52	4.00	7.17	15.81	26.65
	90	15.28	0.99	1.07	7.11	17.04
LYS-B1	50	17.60	6.19	9.50	15.26	21.90
	70	9.26	4.95	6.46	11.33	17.21
	90	20.28	9.14	4.31	4.33	8.69

result of one cyclic loading–unloading of the confining pressure and the increase in temperature from 25 to 50 °C. Therefore, the correlation between the permeability and testing temperature was not fitted using Eq. (6) in this study.

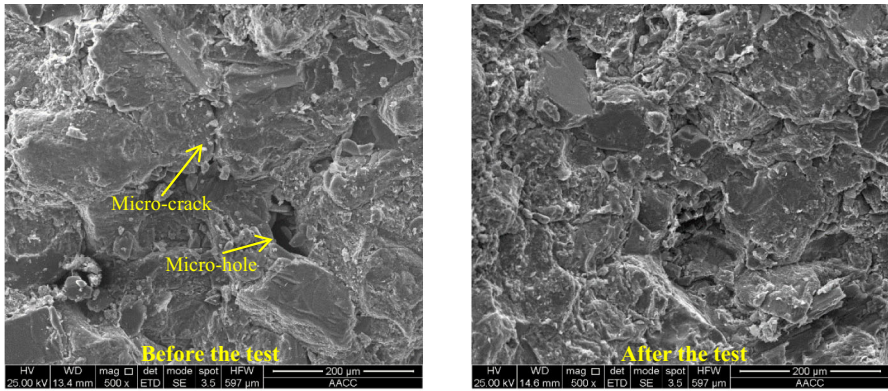
If the permeability reduction was calculated by comparing the value at a low temperature to that under a high temperature in the loading process (e.g., from point i to point iii, Fig. 6a), this could not exactly reflect the temperature influence on the permeability because the reduction was induced by both the external stress and high temperature. Therefore, a damage rate induced by the temperature ( $D_T$ ) was defined in this study to evaluate the reduction in permeability induced by the external temperature, which was calculated by comparing the value at low temperature in the former unloading process to that at a high temperature in the loading process (e.g., from point ii to point iii, Fig. 6a).  $D_T$  is expressed as Eq. (7)

$$D_T = \frac{k_{un} - k_{L1}}{k_{un}} \times 100\%, \quad (7)$$

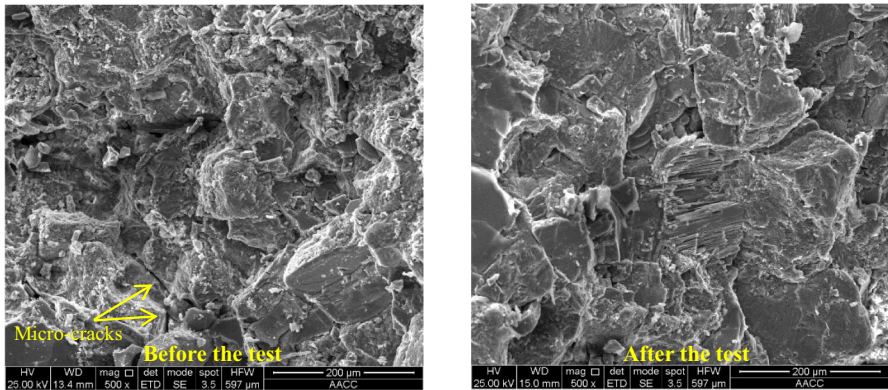
where  $k_{un}$  is the permeability in the unloading process, and  $k_{L1}$  is the permeability in the next loading process.

The values of  $D_T$  under the different testing conditions are listed in Table 4. Table 4 shows that  $D_T$  decreased with increasing testing temperature. This resulted mainly from the temperature effect on the pore structure of the sandstone. As the temperature increased, the pore space in the sandstone specimens increasingly decreased, and therefore, under a high temperature, the reduction rate induced by the testing temperature was lower.

The permeability reduction induced by the rising temperature was a result of the combined effects of rock pore space properties and CO<sub>2</sub> fluid properties. The variation in rock pore properties was mainly due to thermal expansion at elevated temperatures.



(a) Specimen RZS-A1



(b) Specimen RZS-B1

**Fig. 9** Micro-observations of the sandstone in the different temperature treatments

Scanning electron microscopy (SEM) is an effective way to detect the microscopic structure of specimens (Tian et al. 2015; Shakir and Ali 2019). Microscopic observation evidence collected from SEM is shown in Figs. 9 and 10. The tested sandstone materials were all tight, resulting in the corresponding permeability values being low, which were similar to sandstone specimens with a permeability lower than  $10^{-14}$  m<sup>2</sup> (Xu et al. 2018; Xiao et al. 2016). However, before the heating and permeability tests, some microcracks and pores were observed, and the microcracks dominated the sandstone. After the heating and permeability tests, the throats were narrower, and no micropores were observed in the sandstone, which induced a decrement in permeability due to high-temperature treatment. It should be noted that the micro-observations were performed without external stress due to the technical limitations of the microscopy experiment. However, in the permeability test, the rock specimens were heated under a hydrostatic stress of 10 MPa. Under hydrostatic stress conditions, when the thermal stress was below the effective confining pressure, the rock expanded



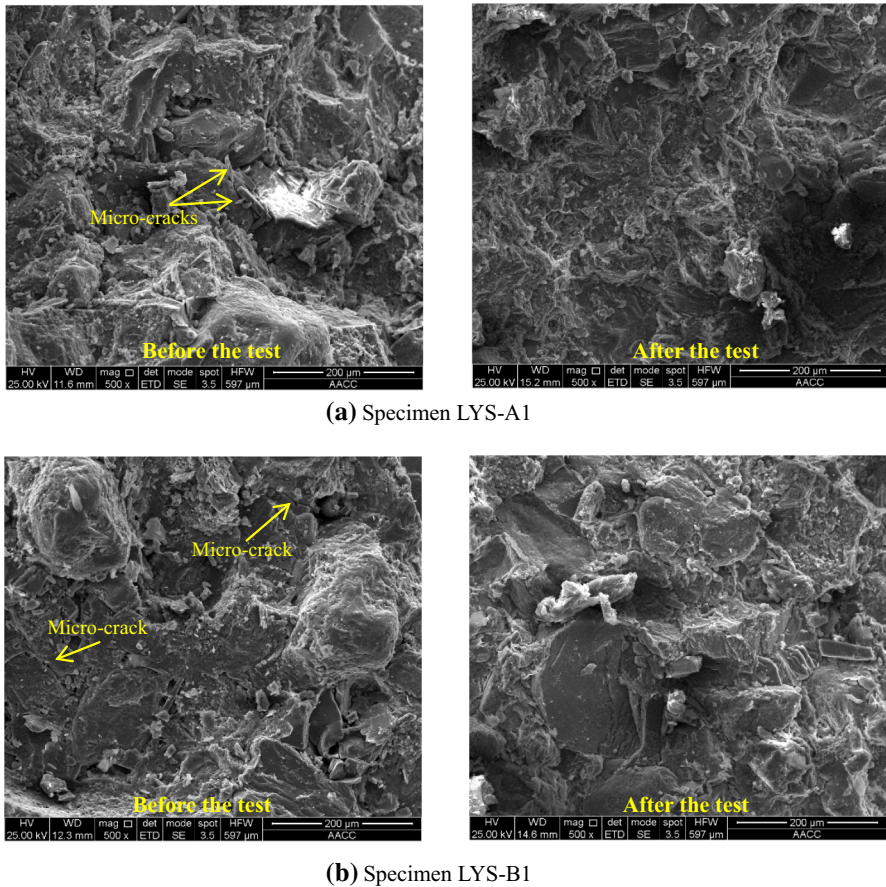


**Fig. 10** Micro-observations of the sandstone in the different temperature treatments

inwards (Li et al. 2009). This indicates that the pore space shrinkage and mineral grain swelling in the permeability test were more significant than those shown in Figs. 9 and 10.

The  $\text{CO}_2$  state in the ranges of the testing temperature and injection pressure used in this study was gaseous according to the  $\text{CO}_2$  phase diagram (De Silva et al. 2017). As the temperature increased from 25 to 90 °C, the dynamic viscosity and adiabatic compressibility of  $\text{CO}_2$  varied. This variation affected Klinkenberg's slip flow of gas (Klinkenberg 1941) and further impacted the sandstone permeability. However, the effect of thermal expansion was predominant in the permeability behavior, and therefore, reductions in permeability were clearly observed when the temperature was increased, as shown in Fig. 7.

## 5 Conclusions

- (i) The confining pressure significantly influenced the permeability of sandstone. As the effective confining pressure increased in the loading process, the permeability of sandstone decreased nonlinearly. The permeability of sandstone in the unloading process was lower compared to that in the loading process, and it increased nonlinearly with the decrease of effective confining pressure. After the confining pressure was unloaded, the sandstone permeability recovery occurred.
- (ii) The permeability of sandstone was affected by the testing temperature, which was observed to decrease with the increase of testing temperature. Moreover, the extent of the permeability reduction induced by the elevated temperature was closely related to the testing temperature. As the testing temperature increased, the percentage reduction in permeability of the sandstone specimens decreased.
- (iii) The mechanism underlying the permeability changes induced by the changes in effective confining pressure and testing temperature was revealed by microscopic observation. Microscopic pore space closure and thermal expansion supported the observed permeability evolution as the confining pressure and temperature were varied. In the loading process of the confining pressure, the pore space decreased, resulting in a decrease in permeability. In the unloading process of the confining process, some of the elastic deformation was recovered, leading to permeability enhancement. Pore space shrinkage and mineral grain swelling resulted in permeability reduction.

**Acknowledgements** This research was supported by the Fundamental Research Funds for the Central Universities (2019QNA04). The authors would like to express their sincere gratitude to the editor and anonymous reviewers for their valuable comments, which have greatly improved this paper.

## Appendix: List of Symbols

$D$	Diameter of specimen
$H$	Height of specimen
$m$	Mass of specimen
$\rho$	Density of specimen
$T$	Temperature
$Q$	Flow rate
$\mu$	Gas viscosity
$A$	Cross-section area
$P_1$	Injection pressures
$P_2$	Downstream pressure
$p_0$	Atmospheric pressure
$\sigma_1$	Axial stress
$\sigma_3$	Confining pressure
$\sigma_e$	Effective confining pressure
$D_k$	Damage rate of permeability
$D_\sigma$	Damage rate induced by stress
$D_T$	Damage rate induced by temperature

$k$	Permeability
$k_0$	Initial permeability
$k_1$	Final permeability
$k_L$	Permeability in the loading process
$k_{un}$	Permeability in the unloading process
$k_{L1}$	Permeability in the next loading process
$a, b, c, d$	Fitting parameters

## References

- Ahmadi MH, Molladavoodi H (2018) Rock failure analysis under dynamic loading based on a micromechanical damage model. *Civil Eng J* 4(11):2801–2812. <https://doi.org/10.28991/cej-03091199>
- Alam AKMB, Niioka M, Fujii Y, Fukuda D, Kodama J (2014) Effects of confining pressure on the permeability of three rock types under compression. *Int J Rock Mech Min Sci* 65(1):49–61. <https://doi.org/10.1016/j.ijrmms.2013.11.006>
- Bachu S (2008) CO<sub>2</sub> storage in geological media: role, means, status and barriers to deployment. *Prog Energy Combust Sci* 34(2):254–273. <https://doi.org/10.1016/j.pecs.2007.10.001>
- Bachu S, Adams JJ (2003) Sequestration of CO<sub>2</sub> in geological media in response to climate change: capacity of deep saline aquifers to sequester CO<sub>2</sub> in solution. *Energy Convers Manag* 44(20):3151–3175. [https://doi.org/10.1016/S0196-8904\(03\)00101-8](https://doi.org/10.1016/S0196-8904(03)00101-8)
- Chen D, Pan Z, Ye Z, Hou B, Wang D, Yuan L (2016) A unified permeability and effective stress relationship for porous and fractured reservoir rocks. *J Nat Gas Sci Eng* 29:401–412. <https://doi.org/10.1016/j.jngse.2016.01.034>
- Cinar Y, Riaz A, Tchelepi HA (2009) Experimental study of CO<sub>2</sub> injection into saline formations. *SPE J* 14(4):1056–1063. <https://doi.org/10.2118/110628-MS>
- David C, Wong TF, Zhu W, Zhang J (1994) Laboratory measurement of compaction-induced permeability change in porous rocks: Implications for the generation and maintenance of pore pressure excess in the crust. *Pure Appl Geophys* 143(1–3):425–456. <https://doi.org/10.1007/BF00874337>
- Davy CA, Skoczylas F, Barnichon JD, Lebon P (2007) Permeability of macro-cracked argillite under confinement: gas and water testing. *Phys Chem Earth* 32(8):667–680. <https://doi.org/10.1016/j.pce.2006.02.055>
- De Silva GPDD, Ranjith PG, Perera MSA, Dai DX, Yang SQ (2017) An experimental evaluation of unique CO<sub>2</sub> flow behaviour in loosely held fine particles rich sandstone under deep reservoir conditions and influencing factors. *Energy* 119:121–137. <https://doi.org/10.1016/j.energy.2016.11.144>
- Ding QL, Ju F, Song SB, Yu BY, Ma D (2016) An experimental study of fractured sandstone permeability after high-temperature treatment under different confining pressures. *J Nat Gas Sci Eng* 34:55–63. <https://doi.org/10.1016/j.jngse.2016.06.034>
- Dong JJ, Hsu JY, Wu WJ, Shimamoto T, Hung JH, Yeh EC, Wu YH, Sone H (2010) Stress-dependence of the permeability and porosity of sandstone and shale from TCDP Hole-A. *Int J Rock Mech Min Sci* 47(7):1141–1157. <https://doi.org/10.1016/j.ijrmms.2010.06.019>
- Ekeleme AC, Agunwamba JC (2018) Experimental determination of dispersion coefficient in soil. *Emerg Sci J* 2(4):213–218. <https://doi.org/10.28991/esj-2018-01145>
- Esmailzadeh A, Behnam S, Mikaeil R, Naghadehi MZ, Saeie S (2017) Relationship between texture and uniaxial compressive strength of rocks. *Civil Eng J* 3(7):480–486. <https://doi.org/10.28991/cej-2017-00000106>
- Forcellini D, Tanganelli M, Viti S (2018) Response site analyses of 3D homogeneous soil models. *Emerg Sci J* 2(5):238–250. <https://doi.org/10.28991/esj-2018-01148>
- Guo X, Zou G, Wang Y, Wang Y, Gao T (2017) Investigation of the temperature effect on rock permeability sensitivity. *J Petrol Sci Eng* 156:616–622. <https://doi.org/10.1016/j.petrol.2017.06.045>
- He YL, Yang LZ (2004) Testing study on variational characteristics of rockmass permeability under loading-unloading of confining pressure. *Chin J Rock Mech Eng* 23(3):415. <https://doi.org/10.3321/j.issn:1000-6915.2004.03.010>

- Huang YH, Yang SQ, Tian WL (2019) Crack coalescence behavior of sandstone specimen containing two pre-existing flaws under different confining pressures. *Theor Appl Fract Mech* 99:118–130. <https://doi.org/10.1016/j.tafmec.2018.11.013>
- Huang YH, Yang SQ, Bu YS (2020a) Effect of thermal shock on the strength and fracture behavior of pre-flawed granite specimens under uniaxial compression. *Theor Appl Fract Mech* 106:102474. <https://doi.org/10.1016/j.tafmec.2020.102474>
- Huang YH, Yang SQ, Hall MR (2020b) Fracture and strain field evolution in faulted brine-saturated sandstone. *J Test Eval* 48(2):1206–1225. <https://doi.org/10.1520/JTE20170524>
- Huang YH, Yang SQ, Li WP, Hall MR (2020c) Influence of super-critical CO<sub>2</sub> on the strength and fracture behavior of brine-saturated sandstone specimens. *Rock Mech Rock Eng* 53:653–670. <https://doi.org/10.1007/s00603-019-01933-2>
- Ju Y, Wang JG, Wang HJ, Zheng JT, Ranjith PG, Gao F (2016) CO<sub>2</sub> permeability of fractured coal subject to confining pressures and elevated temperature: Experiments and modeling. *Sci China Technol Sci* 12:1931–1942. <https://doi.org/10.1007/s11431-016-0478-5>
- Klinkenberg LJ (1941) The permeability porous media to liquids gases. American Petroleum Institute Drilling and Production-Practice. American Petroleum Institute, New York, pp 21–34
- Li XC, Koide H, Ohsumi T (2003) CO<sub>2</sub> aquifer storage and the related rock mechanics issues. *Chin J Rock Mech Eng* 22(6):989–994. <https://doi.org/10.3321/j.issn:1000-6915.2003.06.019>
- Li ZQ, Xian XF, Long QM (2009) Experiment study of coal permeability under different temperature and stress. *J China Univ Min Technol* 38(4):523–527. <https://doi.org/10.3321/j.issn:1000-1964.2009.04.012>
- Liu ZB, Shao JF, Hu DW, Xie SY (2016) Gas permeability evolution with deformation and cracking process in a white marble under compression. *Transp Porous Media* 111(2):441–455. <https://doi.org/10.1007/s11242-015-0603-9>
- Ma D, Duan H, Li X, Li Z, Zhou Z, Li T (2019a) Effects of seepage-induced erosion on nonlinear hydraulic properties of broken red sandstones. *Tunn Undergr Space Technol* 91:102993. <https://doi.org/10.1016/j.tust.2019.102993>
- Ma D, Wang J, Cai X, Ma X, Zhang J, Zhou Z, Tao M (2019b) Effects of height/diameter ratio on failure and damage properties of granite under coupled bending and splitting deformation. *Eng Fract Mech* 220:106640. <https://doi.org/10.1016/j.engfracmech.2019.106640>
- Perera MSA, Ranjith PG, Choi SK, Airey D (2012) Investigation of temperature effect on permeability of naturally fractured black coal for carbon dioxide movement: an experimental and numerical study. *Fuel* 94(1):596–605. <https://doi.org/10.1016/j.fuel.2011.10.026>
- Rathnaweera TD, Ranjith PG, Perera MSA (2015) Effect of salinity on effective CO<sub>2</sub> permeability in reservoir rock determined by pressure transient methods: an experimental study on Hawkesbury sandstone. *Rock Mech Rock Eng* 48(5):2093–2110. <https://doi.org/10.1007/s00603-014-0671-0>
- Rathnaweera TD, Ranjith PG, Perera MSA (2016) Experimental investigation of geochemical and mineralogical effects of CO<sub>2</sub> sequestration on flow characteristics of reservoir rock in deep saline aquifers. *Sci Rep*. <https://doi.org/10.1038/srep19362>
- Scheidegger AE (1958) The physics of flow through porous media. *Soil Sci* 86(6):342–355. <https://doi.org/10.1097/00010694-195812000-00015>
- Shakir AO, Ali HAAR (2019) The effect of lining material on the permeability of clayey soil. *Civil Eng J* 5(3):662–678. <https://doi.org/10.28991/cej-2019-03091277>
- Shi Y, Wang CY (1988) Generation of high pore pressures in accretionary prisms: inferences from the Barbados subduction complex. *J Geophys Res Solid Earth* 93(B8):8893–8910. <https://doi.org/10.1029/jb093ib08p08893>
- Tian X, Cheng L, Cao R, Wang Y, Zhao W, Yan Y, Liu H, Mao W, Zhang M, Guo Q (2015) A new approach to calculate permeability stress sensitivity in tight sandstone oil reservoirs considering micro-pore-throat structure. *J Petrol Sci Eng* 133:576–588. <https://doi.org/10.1016/j.petrol.2015.05.026>
- Wang HL, Xu WY, Cai M, Xiang ZP, Kong Q (2017) Gas permeability and porosity evolution of a porous sandstone under repeated loading and unloading conditions. *Rock Mech Rock Eng* 50(6):2071–2083. <https://doi.org/10.1007/s00603-017-1215-1>
- Xiao W, Li T, Li M, Zhao J, Zheng L, Li L (2016) Evaluation of the stress sensitivity in tight reservoirs. *Petrol Explor Dev* 43(1):115–123. <https://doi.org/10.11698/PED.2016.01.13>
- Xu C, Lin C, Kang Y, You L (2018) An experimental study on porosity and permeability stress-sensitive behavior of sandstone under hydrostatic compression: characteristics, mechanisms and controlling factors. *Rock Mech Rock Eng* 51(8):2321–2338. <https://doi.org/10.1007/s00603-018-1481-6>

- Yang SQ, Huang YH, Tian WL, Zhu JB (2017a) An experimental investigation on strength, deformation and crack evolution behavior of sandstone containing two oval flaws under uniaxial compression. *Eng Geol* 217:35–48. <https://doi.org/10.1016/j.enggeo.2016.12.004>
- Yang SQ, Xu P, Li YB, Huang YH (2017b) Experimental investigation on triaxial mechanical and permeability behavior of sandstone after exposure to different high temperature treatments. *Geothermics* 69:93–109. <https://doi.org/10.1016/j.geothermics.2017.04.009>
- Yu J, Xu W, Jia C, Wang R, Wang H (2019) Experimental measurement of permeability evolution in sandstone during hydrostatic compaction and triaxial deformation. *Bull Eng Geol Env* 78(7):5269–5280. <https://doi.org/10.1007/s10064-018-1425-0>
- Zhang DM, Yang YS, Chu YP, Zhang X, Xue YG (2018) Influence of loading and unloading velocity of confining pressure on strength and permeability characteristics of crystalline sandstone. *Results Phys* 9:1367–1370. <https://doi.org/10.1016/j.rinp.2018.04.043>
- Zhao Y, Qu F, Wan Z, Zhang Y, Liang W, Meng Q (2010) Experimental investigation on correlation between permeability variation and pore structure during coal pyrolysis. *Transp Porous Media* 82(2):401–412. <https://doi.org/10.1007/s11242-009-9436-8>
- Zhou H, Hu D, Zhang F, Shao J, Feng X (2016) Laboratory investigations of the hydro-mechanical-chemical coupling behaviour of sandstone in CO<sub>2</sub> storage in aquifers. *Rock Mech Rock Eng* 49(2):417–426. <https://doi.org/10.1007/s00603-015-0752-8>